# 3D printed porous titanium filled with mineralized UV-responsive chitosan hydrogel promote cell proliferation and osteogenesis in vitro

**Jiazhao Yang**
The First Hospital of USTC, University of Science and Technology of China
**Changshun Zhou**
College of Life Sciences and Medicine,Zhejiang Sci-Tech University
**Fan Liu**
School of Stomatology,China Medical University
**Hejie Li**
Institute of Laser Advanced Manufacturing,zhejiang University of Technology
**Gaolin Yang**
Institute of Laser Advanced Manufacturing,Zhejiang University of Technology
**Shiyuan Fang**
The First Hospital of USTC, University of Science and Technology of China
**In-seop Lee**
Institute of Human Materials
**Cen Chen** ( chencen@zstu.edu.cn )
Zhejiang Sci-Tech University

**Research Article**

**Keywords:** porous Titanium, chitosan, ultraviolet (UV)-responsive, mineralization, osteogenesis

**Posted Date:** March 18th, 2022

**DOI:** https://doi.org/10.21203/rs.3.rs-1380937/v1

# Abstract

**Background:** The modification of 3D printed porous titanium (Ti) have received significant attention to promote its osteogenesis for clinical use.

**Methods:** Ultra-violet (UV) responsive chitosan (CSMA), as an injectable filling material, was incorporated into porous Ti, and *in situ* mineralized by carbon oxide ($CO_2$) diffusion to form mineralized CSMA (CSMA/$CaCO_3$). Physiochemical and biological properties were investigated *in vitro* .

**Results:** CMSA/$CaCO_3$ exhibited porous morphology and favorable biocompatibility, which could promote adhesion and proliferation of bone mesenchymal stem cells (BMSCs). Moreover, the release of $Ca^{2+}$ from $CaCO_3$ particles could increase alkaline phosphatase (ALP) activities, up-regulate osteopontin (OPN) and osteocalcin (OCN) expression levels, and enhance extracellular mineralization of BMSCs.

**Conclusions:** 3D printed porous Ti filling with mineralized UV-responsive chitosan hydrogel could promote proliferation and osteogenesis of BMSCs, and have great potential for Ti implant modification in bone tissue engineering.


# 1. Introduction

Titanium (Ti) and its alloys have been widely applied for biomedical application due to their superior physicochemical properties and biocompatibilities for last several decades [1, 2]. The fabrication of porous Ti implants by 3D printing technology are catching the interests as the strategy for hard tissue replacement, which could effectively avoid stress shielding, control mechanical properties to targeted implantation area and favor bone ingrowth [3–6].

Somehow, bioinert Ti implants cannot induce enough bone regeneration, resulting in nearly 10% failure rate of hard tissue replacement in clinic treatment [7, 8]. Surface modification methods (i.e. electrochemical deposition, biochemical coating and chemical vapor deposition) are necessary to improve physicochemical properties of Ti, as well as forming fast fixations and chemical bonds with bones [9, 10]. Calcium -based minerals, such as calcium phosphate and calcium carbonate ($CaCO_3$) are widely used for surface modification owing to their favorable osteoinductivity. However, the traditional methods to deposit mineral coating, including micro-arc oxidation, electro-deposition and hydrothermal treatment, mainly focus on modifying the surfaces, rather than entire pore structures [11–13]. Inner pore structures could not only control the mechanical properties of Ti implants to match with surrounding tissues, but also facilitate cell adhesion and tissue ingrowth.

Recently, stimulate-responsive hydrogels, which can undergo reversible or inversible phase transition *in situ* by light, heat, magnetism and/or force stimulation, have received significant attention as the filling materials for porous Ti implants [14–16]. Among them, the phase transition of photo-responsive hydrogels allows fast gelation and injection *in situ*. The precisely spatiotemporal control of photo-responsive hydrogels could regulate encapsulated drug/protein release and activate cell behaviors [5, 17,

18]. Chitosan (CS), derived from chitin, is a natural polysaccharide with controllable biodegradability and favorable biocompatibility. Methacrylic anhydride (MA) can interact with amidogen of CS through acylation reaction, resulting in the formation of photo-responsive CSMA under UV radiation [5, 16, 19].

In previous study, an *in situ* mineralization method was developed to fabricate a $CaCO_3$ layer at the hydrogel-titanium interfaces by carbon oxide ($CO_2$) diffusion [20]. The calcium chloride was firstly added into hydrogels, which were placed on Ti substrate. Then $CO_2$ phase was introduced to hydrogels by decomposition of $(NH_4)_2CO_3$ powders. The $Ca^{2+}$ in hydrogel were reacted with negatively charged $CO_3^{2-}$ ions to form $CaCO_3$ layer near the vapor/hydrogel interface. Therefore, it is reasonable to presume that, the pore structure of 3D printed Ti could be modified with mineralized hydrogel via similar procedure.

In present study, porous Ti was firstly filled with UV-responsive chitosan hydrogel. Then the *in situ* mineralization by $CO_2$ diffusion was employed to grow $CaCO_3$ particles within hydrogel. We hypothesized that this porous Ti filled with mineralized chitosan hydrogel will release $Ca^{2+}$ continuously, resulting in promoted proliferation and osteogenesis of bone marrow mesenchymal stem cells (BMSCs) *in vitro* (Scheme 1).

## 2. Materials And Methods

# 2.1 Fabrication of 3D printed Ti discs

Porous Ti discs were fabricated by selective laser melting (SLM) system (EOSINT-M280, EOS GmbH, Munich, Germany) as previous described [21]. sample was designed by Solidworks software and saved as a STL file. Laser beam scanning (speed: 700 mm/s, power: 400 W) was utilized to fuse the powder together to generate a desired 2D layer. Subsequently, a new layer of powder was spread, and the process was repeated until the whole construct had been built. After printing, samples were ultrasonically cleaned with acetone, ethanol and deionized water twice. Two types of samples were fabricated: 1) bullet-shaped cages with open window for clear observation of CSMA hydrogels; 2) discs with 800 μm pore size, 70% porosity (Ø10 mm × L3 mm) for further use.

# 2.2 Synthesis of UV responsive CSMA

Chitosan powder (Macklin Biochemical Co.,Ltd, Shanghai, China) was firstly dissolved into 100 mL 1% (v/v) acetic acid solution to obtain 1% (w/v) chitosan solution. Methacrylic anhydride solution (Macklin, Shanghai, China) was slowly dropped into well-dissolved chitosan solution, kept stirring under 60°C for 12 h, and then adjusted to pH = 7 by adding $Na_2CO_3$ (Sigma Aldrich, Darmstadt, Germany) to terminate the reaction. The mixture was dialyzed for another three days, and lyophilized to obtain CSMA powders. 1% (w/v) CSMA solution were prepared by dissolving CSMA powders into deionized water, and underwent evaporating to obtain 2% and 3% (w/v) CSMA solution.

# 2.3 Preparation of porous Ti filled with mineralized chitosan hydrogel

The printed porous Ti discs were heated in alkali solution to provide Ti-OH sites, according to previous procedure [22]. Three different groups were prepared as follows, 1) 200 μL 2% CSMA solution with 0.2 wt% photoinitiator (I2959, Aladdin, Shanghai, China) were premixed and injected into alkali-treated Ti discs, followed by UV irration (GGY250, Wuxi Changya Lighting Co., Ltd, Wuxi, China) for 3 mins, denoted as CSMA. 2) CSMA solution with I2959 were immersed into 4 M $CaCl_2$ solution (Sigma Aldrich, Darmstadt, Germany), and kept stirring for 2 h. 200 μL mixture was injected into alkali-treated Ti discs, and crosslinked by UV irradiation for 3 min, known as CSMA/$CaCl_2$. 3) Mineralization of CSMA/$CaCl_2$ was proceeded by $CO_2$ diffusion (Scheme 1). $(NH_4)_2CO_3$ (Macklin Biochemical Co.,Ltd, Shanghai, China) in the specific apparatus was decomposed into $CO_2$ and $NH_4$ gas in room temperature. $CO_2$ was diffused into CSMA/$CaCl_2$ mixture, and reacted with $Ca^{2+}$ to obtain CSMA/$CaCO_3$.

# 2.4 Characterization of porous Ti filled with CMSA-based hydrogels

## 2.4.1 Physical-chemical parameters

The microstructure of CSMA-based hydrogels (CSMA, CSMA/$CaCl_2$ and CSMA/$CaCO_3$) were observed by scanning electron microscope (SEM, Quanta 200, FEI Company, Philips, Netherlands). All lyophilized samples were sputter-coated with gold using ion sputter. SEM images were obtained at magnification of × 500. The chemical compositions of CSMA-based hydrogels were characterized by AIR-FTIR (Nicolet IS50, ThermoFisher Scientific, Massachusetts, America) and XRD (Philips PW1700, Philips, Amsterdam, Netherlands). The AIR-FTIR spectra were recorded from 500–4000 $cm^{-1}$ with a 2 $cm^{-1}$ resolution and 20 scans. XRD analysis was performed using a Cu-Kα source (λ = 1.54 nm) at 40 kV, and the spectrum were recorded from 10 to 60° of 2 theta.

Thermal behaviors of CSMA-based hydrogels were performed by using thermogravimetric analysis (TGA, NAICHI scientific instruments trading Co., Ltd, Shanghai, China). All lyophilized samples were undergoing thermal scanning conditions (30–800°C).

## 2.4.2 Release kinetics of calcium ions and loaded drug

The release profile of calcium ions ($Ca^{2+}$) in mineralized CSMA were measured by using QuantiChrom™ calcium assay kit (DICA-500, BioAssay Systems, USA). In detail, CSMA/$CaCl_2$ and CSMA/$CaCO_3$ hydrogels (1% and 3%) with were immersed into PBS solution at 37°C for determined periods up to 14 days. At each time points, the released $Ca^{2+}$ ions in the collected supernatants were measured according to the protocol [23].

In order to investigate the loading/release capability of CMSA-based hydrogels, rhodamine (Macklin Biochemical Co.,Ltd, Shanghai, China) was selected as model drug which was incorporated into CSMA-based hydrogels due to its fluorescence characteristic, and detected by using UV spectrophotometer (UV-1800PC, Shanghai Meipuda instrument Co., Ltd, Shanghai, China). Briefly, 0.1 mg/mL rhodamine solution

were added into CSMA and CSMA/$CaCl_2$ prepolymer solution, and crosslinked by UV irradiation for 3 min. In term of CSMA/$CaCO_3$, $CO_2$ diffusion was similarly proceeded after incorporation of rhodamine. All samples were immersed into physiological saline solution, and incubated at 37°C for 14 days. At planned time point, supernatant was collected, and measured at 485 nm.

## 2.5 Cell culture

Bone marrow mesenchymal cells (BMSCs) (Cyagen Biosciences, Guangzhou, China) were cultured in growth medium (BMSCs basal medium, 10% fetal bovine serum (FBS) and 1% antibiotic-antimycotic) at 37°C. The culture medium was changed every 3 days until the cells reached 80–100% confluence. The third to fifth passages were used to evaluate cell adhesion, proliferation, and osteogenic differentiation.

## 2.6 Cytotoxicity and osteogenesis of BMSCs *in vitro*

### 2.6.1 In-direct cytotoxicity

The in-direct cytotoxicity of 3D printed porous Ti filled with CSMA-based hydrogels was investigated based on the international standard ISO 10993-5. The leach liquor of all samples was collected after 3-day incubation in growth medium at 37°C. BMSCs were cultured in leach liquor at a density of $5 \times 10^4$ /mL for 24 h and 48 h. Growth medium was used as the negative control, which was regarded as “cell viability = 100%”. Positive control referred to growth medium with 0.64% phenol solution. At planned time point, cells were washed by PBS solution, then fresh culture medium (200 μL) with 20 μL of CCK-8 reagent (Beyotime Biotechnology, Shanghai, China) were added to each sample, incubated at 37°C for 1 h, and measured at 450 nm using microreader (TECAN DNA Export, TECAN, Manedov, Switzerland). Meanwhile, calcein-AM/PI (Beyotime Biotechnology, Shanghai, China) staining was further used to observe live/dead cells. At the planned time point, the samples were washed with PBS solution. 500 μL staining solution were added to each sample, and incubated at 4°C for 20 min in the dark. After being washed by PBS solution, samples were observed under a confocal microscope (IX81-FV1000, Olympus, Tokyo, Japan).

### 2.6.2 Cell proliferation and cellular morphology

$2 \times 10^4$/mL cells were seeded on well-prepared samples (CSMA, CSMA/$CaCl_2$ and CSMA/$CaCO_3$), and cultured for 14 days. At planned time point, cell proliferation rates was investigated by using CCK-8 kit, according to the protocol above.

To evaluate cell adhesive ability, cell morphologies and skeleton were stained by rhodamine-conjugated phalloidin (Beyotime Biotechnology, Shanghai, China). Briefly, $4 \times 10^5$ cells were cultured in well-prepared CSMA-based hydrogels for 24 h and fixed with 4% paraformaldehyde solution for 10 min and permeabilized using 0.5% Triton X-100 in PBS for 5 min. After being washed with PBS for 10 min twice, cells were incubated with rhodamine-conjugated phalloidin for 30 min in the dark followed by counterstaining with 4',6-diamidino-2-phenylindole (DAPI) to visualize the nuclei. Images were captured with a confocal microscope.

## 2.6.3 Osteogenesis of BMSCs

Osteogenesis of BMSCs cultured in CSMA-based hydrogels were performed by evaluating alkaline phosphatase (ALP) activities, osteogenesis-related genes expression levels and extracellular mineralization. Osteogenic medium was used to stimulate osteogenic differentiation, which was composed of BMSCs basal medium, 10% fetal bovine serum, 1% antibiotic-antimycotic, 3 mmol/L β-glycerophosphate, 50 μg/mL ascorbic acid and 1 μmol/L dexamethasone. Mineralizing medium referred to osteogenic medium without dexamethasone (Dex). Cells were cultured on 48-well tissue culture plate (TCP) in growth medium, denoted as negative control, while positive control referred to cells seeded on TCP in osteogenic medium.

## 2.6.3.1 ALP activity

BMSCs at the density of $2\times10^4$/mL were transferred to well-prepared 3D printed porous Ti filled with CSMA-based hydrogels and cultured in growth medium to reach 60–70% confluence. Then, the medium was changed to mineralizing medium. ALP activities of BMSCs were measured by using ALP assay kit (Beyotime, Shanghai, China) based on the color reaction of colorless p-nitrophenyl phosphate (pNPP) converted to yellow p-nitrophenol after incubation at 37°C [24]. At day 5, 7 and 14, cells on each sample were washed by PBS solution twice, and lysed by using RIPA lysis buffer solution (Sigma Aldrich, Darmstadt, Germany). After centrifugation at 5000 rpm for 10 min, the supernatant was transferred into 96-well plate. The substrates and p-nitrophenol were added in sequence and incubated at 37°C for 30 min. Finally, the reaction was stopped by the addition of 100 μL stop buffer and the absorbance at 405 nm was measured. ALP activity was calculated from a standard curve after normalizing to the total protein content, which was measured using the BCA Protein Assay Kit (Sigma Aldrich, Darmstadt, Germany). ALP activity was expressed as nmol of p-nitrophenol formation/min/mg of total proteins.

## 2.6.3.2 Osteogenesis-related gene expression of BMSCs

Osteocalcin (OCN) and osteopontin (OPN) are representative osteogenesis-related gene markers. Quantitative real-time reverse transcription polymerase chain reaction (RT-PCR) was performed to evaluate the OPN and OCN expression levels of BMSCs in 3D printed porous Ti filled with CSMA-based hydrogels at day 5, 7 and 14. At each time point, the total RNA from each sample was first extracted using TRIzol solution (Sigma Aldrich, Darmstadt, Germany), and the concentration was determined with the spectrophotometer (UV-1800PC, Shanghai Meipuda instrument Co., Ltd, Shanghai, China). The primer sequences used for PCR amplification are listed in Table 1. The gene expression levels were calculated using the $2 - \Delta\Delta CT$ method.

Table 1
Primers for RT-PCR

| Genes | Forward primer | Reverse primer |
|---|---|---|
| OCN | CTCACTCTGCTGGCCCTGAC | CACCTTACTGCCCTCCTGCTTG |
| OPN | CAAGGTCATCCCAGTTGCCCAG | GCTTTGGAACTCGCCTGACTGTC |
| GAPDH | GAAGGTCGGTGTGAACGGATTTG | CATGTAGACCATGTAGTTGAGGTCA |

### 2.6.3.3 Alizarin red staining

Furthermore, Alizarin red staining kit (Cyagen Biosciences, Guangzhou, China) was used to evaluate extracellular deposition and mineralization of BMSCs in the presence of 3D printed porous Ti filled with CSMA-based hydrogels. Briefly, at day 28, cells were fixed using 10% neutral formalin. After washing three times with distilled water, the Alizarin red staining solution was added and incubated at room temperature for 30 min. The excess dye was removed, samples were imaged using an inverted microscope equipped with a digital camera (Nikon, Tokyo, Japan).

## 2.4. Statistical analysis

All quantitative data were obtained from two or more independent experiments with triplicate or quadrant repeats and expressed as the mean ± standard deviation. A one-way ANOVA followed by Tukey's test or Student-Newman-Keuls test was used to the statistical analysis among different groups.

# 3. Results And Discussion

## 3.1 Structural characterization

Bullet-shaped cages with open window were prepared in order to have clear observation on pore structures filled with CSMA-based hydrogels (Fig. 1). Pores were obviously filled with solidified CSMA hydrogels, while the transparent hydrogels became turbid with incorporation of inorganic particles in CSMA/$CaCO_3$. From SEM images (Fig. 2A), all CSMA displayed similar microporous morphologies and good connectivity between the pores. The pore sizes of CSMA hydrogels with 1%, 2% and 3% w/v were 283 ± 13.98, 254 ± 27.03 and 153.70 ± 13.25 μm, respectively. 1% and 3% CSMA hydrogels were selected for porous Ti modification in further research. As shown in Fig. 2B, the morphology of CSMA/$CaCl_2$ was flat, while CSMA/$CaCO_3$ reappeared porous structure with particles deposition. Minerals were aggregated and randomly distributed into CSMA. We speculated the $CaCl_2$ had favorable water-absorption ability, the abundant water collapsed the formed porous structure of CSMA, resulting in flat surface. In the process of mineralization by $CO_2$ diffusion, organic particles supported the whole structure and enhanced hydrogel stability, resulting in the morphological differences between CSMA/$CaCl_2$ and CSMA/$CaCO_3$.

XRD pattern of CSMA-based hydrogels was shown in Fig. 2C. A blunt and broad peak located at 20.3° corresponding to low crystalline phase of hydrogen bonds in CSMA hydrogels, resulting from N-acylation.

No obvious variations were observed for CSMA/$CaCl_2$, indicating the introduction of $CaCl_2$ had no influence on CSMA chemical structure. In term of CSMA/$CaCO_3$, the characteristic peaks occurred at 23.5° and 29.7°, which matched the standard $CaCO_3$ JCPDS card. Two minor peaks at 32.5° and 58.6° represented the charactertiscs of $NH_4Cl$. To be specific, $NH4^+$ was generated by the decomposition of $(NH_4)_2CO_3$ gas, and combined with $Cl^-$ ions, which was in accordance with the process of mineralization by diffusion of $CO_2$ [20].

In AIR-FTIR spectrum (Fig. 2D), CSMA exhibited representative peaks at 1655 $cm^{-1}$, 1547 $cm^{-1}$ and 1314 $cm^{-1}$, corresponding to amide I band (C = O stretching vibration), the amide II band (NH deformation vibration and CN Stretching vibration) and amide III, respectively. No obvious bands were found in the range of 1730–1740 $cm^{-1}$ (ester group), indicating the acylation reaction was proceeded between chitosan amino group and methacrylic anhydride, rather than hydroxyl group of chitosan and methacrylic anhydride. The peak at 1669 $cm^{-1}$ represented the formation of $CaCl_2$ in CSMA/$CaCl_2$ samples. In CSMA/$CaCO_3$ hydrogels, $Ca^{2+}$ existed in the form of calcite. The characteristic peak at 1407 $cm^{-1}$ (CO antisymmetric stretching vibration), 831 $cm^{-1}$ ($CO_3^{2-}$ surface External deformation vibration) and 719 $cm^{-1}$ (O-C-O in-plane deformation vibration) further demonstrated $CaCO_3$ was synthesized by the reaction of $CO_2$ and $Ca^{2+}$.

Thermal behaviors of CSMA-based hydrogels were shown in Fig. 2E. The weight loss of samples was mostly attributed to water evaporation under 100°C. CSMA/$CaCl_2$ approximately lost 60% weight due to its high hydrophilicity, while nearly 10% weight lost were observed in CSMA and CSMA/$CaCO_3$ from 30–100°C. In second phase (100°C-460°C), CSMA and CSMA/$CaCO_3$ samples firstly kept the same rates of weight loss. Nerveless, CSMA exhibited a higher weight loss velocity as temperature increasing that possibly resulted from the accelerated degradation of organic components, and left 30% residual weight. In term of CSMA/$CaCO_3$, the inorganic particles could stabilize the entire structure under persistently increasing temperature, which 48% weight were remained in CSMA/$CaCO_3$. The collapsion and degradation of $CaCO_3$ particles resulted in the ultimate weight loss (20%) at 700°C.

The release kinetics of $Ca^{2+}$ ions were shown in Fig. 3. Generally, all samples had rapid $Ca^{2+}$ release profile in the first 24 h, and followed by gentle release until 14 days. CSMA/$CaCl_2$ had higher release rate and larger accumulated amount of $Ca^{2+}$ ions than those of CSMA/$CaCO_3$, no matter in 1% or 3% CSMA. We speculated the differences were attributed to the existing form of calcium. Free $Ca^{2+}$ ions were easily diffused from the CSMA/$CaCl_2$. Whereas, the releasing of $Ca^{2+}$ ions from CSMA/$CaCO_3$ depended on the degradation of sparingly soluble $CaCO_3$. Besides, 1% CSMA/$CaCO_3$ had higher release velocities when compared with 3% samples. From SEM observation, 1% CSMA/$CaCO_3$ exhibited larger pore sizes than those of 3% CSMA/$CaCO_3$. However, no significant differences were found between 1% and 3% CSMA/$CaCl_2$, probably due to the similar surface morphologies.

## 3.2 *In vitro* biocompatibility of porous Ti filled with CSMA-based hydrogels

The in-direct cytotoxicity of 3D printed porous Ti filled with CSMA-based hydrogels was shown in Figure S1. Generally, Cell viabilities increased in higher CSMA concentration. In 24 h, cell viabilities in 1% CSMA and 1% CSMA/$CaCO_3$ samples were significantly lower than that of 1% CSMA/$CaCl_2$ ($P < 0.05$), while no differences were found among three 3% CSMA-based hydrogels. Similar trends of cell viabilities were observed in 48 h, 3% CSMA/$CaCO_3$ displayed the highest cell viability ($P < 0.05$). Meanwhile, the results of cell viabilities in the live/dead staining were in accordance with CCK-8 results above (Fig. S2), indicating all CSMA-based hydrogels presented favorable biocompatibility.

The initial cell adhesion and proliferation at material-tissue interface play a crucial role in the early stage of bone formation. As shown in Fig. 4A, cells were randomly distributed in all samples. Among them, more BMSCs with bright blue nuclei and red cytoskeleton were observed within 3% CSMA/$CaCO_3$. Lee *et al*. demonstrated that porous structure with rough surface morphologies easily activated the formation of focal adhesions and ordered distribution of stress fibers, which were beneficial for osteoblasts initiative adhesion and colonization [25]. Additionally, the released $Ca^{2+}$ could facilitated extracellular matrix secretion, as well as providing adsorption sites for adhesion protein (i.e. collagen, fibronectin) [26]. Thus, 3D printed porous Ti with CSMA/$CaCO_3$ displayed favorable cell affinity.

BMSCs proliferation within porous Ti filled with CSMA-based hydrogels were shown in Fig. 4B. In general, all samples displayed more cell proliferation with time increasing. 3% CSMA-based hydrogels had higher cell proliferation than those of 1% CSMA-based hydrogels. No significant differences were found between CSMA and CSMA/$CaCl_2$ at each time point, no matter in 1% or 3% w/v concentration. At day 3, cell proliferation in CSMA/$CaCO_3$ were significantly higher than those in the rest of samples ($P < 0.05$), and kept persistently increasing until the 14th day. It was suggested that $Ca^{2+}$ released from CSMA/$CaCO_3$ could promote cell proliferation [27]. 3% w/v CSMA/$CaCO_3$ exhibited the highest proliferation rate among all samples, due to the continuous release of $Ca^{2+}$. However, CSMA/$CaCl_2$ performed a burst release of $Ca^{2+}$ in first few days, along with medium change every 3 days, the residual $Ca^{2+}$ in CSMA/$CaCl_2$ insufficiently activated more cells, resulting in the similar proliferation rates with CSMA.

## 3.3 BMSCs osteogenesis within porous Ti filled with mineralized CSMA

During implantation surgery, progenitors and inflammatory cells migrate and initiate healing process [28]. Bone formation relies on the recruitment of MSCs, which could differentiate osteoblasts. Osteogenic differentiation of BMSCs is necessary for bone matrix synthesis and mineralization, which plays an important role in osteointegration between Ti and surrounding tissues. ALP activity is regarded as a marker of early-stage of osteogenic expression [29]. OPN and OCN are not only non-collagenous proteins present in bone matrix, but also known as important secretory proteins that regulated downstream

osteogenesis-related gene expression [30, 31]. The extracellular deposition and mineralization is determined by calcium nudes, known as late-stage marker of BMSCs osteogenesis [32]. To our knowledge, osteogenic medium is considered as gold standard for cell osteogenic-induced differentiation. Dexamethasone (Dex), one of steroid hormones, has been applied along with ascorbic acid and β-glycerophosphate as important ingredients in osteogenic medium that could induce osteogenic differentiation of MSCs *in vitro* [33]. Thus, porous Ti filled with mineralized CSMA were cultured in mineralizing medium, while positive control cultured in osteogenic medium. The osteogenesis of all samples was further investigated by evaluating ALP activities, OCN and OPN expression levels, and calcium nudes.

As shown in Fig. 5A, ALP activity in positive control kept increasing and reached its maximum at day 7, and followed by decreasing at day 14, which were in accordance to previous research [34]. Due to lack of Dex in mineralizing medium, Ti and negative control exhibited significantly lower ALP activities at each time point when compared with positive control ($P < 0.05$). In term of CSMA/$CaCO_3$, ALP activities on CSMA/$CaCO_3$ (1% and 3%) reached the highest levels at day 5, which were significantly higher than positive control ($P < 0.05$). More importantly, the rapid increase of ALP activity in 3% CSMA/$CaCO_3$ at day 5 even slightly higher than that in positive control at day 7, indicating 3% CSMA/$CaCO_3$ could effectively stimulate and improve osteogenesis of BMSCs by significantly up-regulated ALP activity in advance.

Next, the osteogenic genes related to CSMA/$CaCO_3$-induced BMSCs were primarily investigated by RT-PCR. As shown in Fig. 6A, CSMA/$CaCO_3$ exhibited the highest OPN levels at day 5 ($P < 0.05$). Meanwhile, OPN levels on 3% CSMA/$CaCO_3$ were up-regulated the most until day 7, which were 1.5-fold higher than that in positive control. Although OPN levels on CSMA/$CaCO_3$ slightly decreased at day 14, no differences were found between CSMA/$CaCO_3$ and positive control ($P < 0.05$). In term of OCN level (Fig. 5B), positive control exhibited highest OCN level ($P < 0.05$) at day 5, and kept increasing until day 7. However, OCN levels on CSMA/$CaCO_3$ kept persistently increasing, and reached the maximum at day 14. In particular, 3% CSMA/$CaCO_3$ presented almost 2-fold higher OCN levels when compared with positive control ($P < 0.05$). Furthermore, alizarin red staining is determined for calcium mineralization. As shown Fig. 5B, it was noted that cell-free samples displayed red colour due to the presence of $Ca^{2+}$ in CSMA/$CaCO_3$. Red nodules could be obviously observed in CSMA/$CaCO_3$ when compared with Ti samples at day 28, indicating mineralized CSMA promoted osteogenesis of BMSCs. Therefore, it was demonstrated that both 1% and 3% CSMA/$CaCO_3$ could induced osteogenic differentiation of BMSCs by up-regulating OPN and OCN expression levels, and enhancing extracellular deposition and mineralization.

In summary, porous Ti filled with mineralized CSMA exhibited favorable biocompatibility, and effectively enhanced osteogenesis of BMSCs *in vitro*. The obvious osteogenesis effect of CSMA/$CaCO_3$ was determined by $CaCO_3$ particles in mineralized CSMA, rather than free $Ca^{2+}$. In the process of $CaCO_3$ degradation, the continuous release of $Ca^{2+}$ regulate the osteocyte differentiation by activating ERK1/2 and PI3K/Akt pathways [35, 36]. Besides, $Ca^{2+}$ could occupy the majority of the acidic residues within

OPN, which were highly involved in hydroxyapatite crystal and deposition [37]. Therefore, mineralized CSMA was considered as an excellent osteoinductive carrier that could incorporate into entire pore structures of Ti. Additionally, fast gelation *in situ* is another advantage of UV-responsive chitosan, indicating CMSA could load proteins/drugs *in situ*, and release them in a controllable manner. Thus, rhodamine was selected as model drug which was incorporated into CSMA-based hydrogels. From Figure S3, release velocity increased in lower CSMA concentration. 3% CSMA/$CaCO_3$ presented a burst release in first few hours, and kept slowly releasing for a week.

# 4. Conclusions

In present study, mineralized UV-responsive chitosan was filled into 3D printed porous Ti by $CO_2$ diffusion. CSMA/$CaCO_3$ promoted BMSCs adhesion and proliferation, which displayed the favorable biocompatibility. Moreover, 3% CSMA/$CaCO_3$ could increase ALP activities in advance, up-regulate OPN and OCN levels by 1.5-fold and 2-fold respectively, as well as enhancing extracellular matrix mineralization, indicating 3D printed porous Ti implants filled with mineralized CSMA could effectively promoted osteogenesis of BMSCs, which was considered as an effective and novel modification strategy for bone regeneration.

# Declarations

### Ethics approval and consent to participate

Not applicable

### Consent for publication

Not applicable

### Availability of data and materials

Not applicable

### Competing interests

The authors declare that they have no competing interest.


### Funding

Not applicable


### Authors' contributions

CC and YJZ is responsible for modifying the manuscript. ZCS and LF was responsible for initial literature review and writing of the manuscript. ISL and FSY made some pertinent suggestions. LHJ and YGL

contributed to the completion of the manuscript. All authors read and approved the final manuscript.

### Acknowledgements

This research was supported partly by Zhejiang Provincial Natural Science Foundation of China (LY20E010006), partly by the Fundamental Research Funds for the Central Universities (WK9110000152) and partly by National Natural Science Foundation of China (51502265, 81701033).

# References

1. Ottria L, Lauritano D, Andreasi Bassi M, Palmieri A, Candotto V, Tagliabue A, Tettamanti L. Mechanical, chemical and biological aspects of titanium and titanium alloys in implant dentistry. J Biol Regul Homeost Agents. 2018;32:81–90.
2. Chen S, Tsoi JKH, Tsang PCS, Park Y-J, Song H-J, Matinlinna JP. Candida albicans aspects of binary titanium alloys for biomedical applications. Regenerative biomaterials. 2020;7:213–20.
3. Popov VVJ, Muller-Kamskii G, Kovalevsky A, Dzhenzhera G, Strokin E, Kolomiets A, Ramon J. Design and 3D-printing of titanium bone implants: brief review of approach and clinical cases. Biomed Eng Lett. 2018;8:337–44.
4. Ma L, Wang X, Zhao N, Zhu Y, Qiu Z, Li Q, Zhou Y, Lin Z, Li X, Zeng X, et al. Integrating 3D Printing and Biomimetic Mineralization for Personalized Enhanced Osteogenesis, Angiogenesis, and Osteointegration. ACS Appl Mater Interfaces. 2018;10:42146–54.
5. Wu K, Liu M, Li N, Zhang L, Meng F, Zhao L, Liu M, Zhang Y. Chitosan-miRNA functionalized microporous titanium oxide surfaces via a layer-by-layer approach with a sustained release profile for enhanced osteogenic activity. J Nanobiotechnol. 2020;18:127.
6. Zheng Y, Han Q, Wang J, Li D, Song Z, Yu J. Promotion of Osseointegration between Implant and Bone Interface by Titanium Alloy Porous Scaffolds Prepared by 3D Printing. ACS biomaterials science & engineering. 2020;6:5181–90.
7. Nelson KL, Cox MD, Richter GT, Dornhoffer JL. A Comparative Review of Osseointegration Failure Between Osseointegrated Bone Conduction Device Models in Pediatric Patients. Otology & neurotology: official publication of the American Otological Society American Neurotology Society [and] European Academy of Otology and Neurotology. 2016;37:276–80.
8. Smith AJ, Dieppe P, Vernon K, Porter M, Blom AW. Failure rates of stemmed metal-on-metal hip replacements: analysis of data from the National Joint Registry of England and Wales. Lancet (London England). 2012;379:1199–204.
9. Souza JCM, Sordi MB, Kanazawa M, Ravindran S, Henriques B, Silva FS, Aparicio C, Cooper LF. Nano-scale modification of titanium implant surfaces to enhance osseointegration. Acta Biomater. 2019;94:112–31.
10. Bosshardt DD, Chappuis V, Buser D. Osseointegration of titanium, titanium alloy and zirconia dental implants: current knowledge and open questions. Periodontol 2000. 2017;73:22–40.

11. Ribeiro AR, Oliveira F, Boldrini LC, Leite PE, Falagan-Lotsch P, Linhares ABR, Zambuzzi WF, Fragneaud B, Campos APC, Gouvêa CP, et al. Micro-arc oxidation as a tool to develop multifunctional calcium-rich surfaces for dental implant applications. Mater Sci Eng C Mater Biol Appl. 2015;54:196–206.
12. Hadzima B, Mhaede M, Pastorek F. Electrochemical characteristics of calcium-phosphatized AZ31 magnesium alloy in 0.9% NaCl solution. J Mater Sci: Mater Med. 2014;25:1227–37.
13. Vishnu J, Manivasagam K, Gopal V, Bartomeu Garcia V, Hameed C, Manivasagam P, Webster G. T.J. Hydrothermal treatment of etched titanium: A potential surface nano-modification technique for enhanced biocompatibility. Nanomedicine: Nanatechnol biology Med. 2019;20:102016.
14. Zhang QG, Hu WW, Zhu AM, Liu QL. UV-crosslinked chitosan/polyvinylpyrrolidone blended membranes for pervaporation. RSC Adv. 2013;3:1855–61.
15. Zheng Z, Zhou T, Hu R, Huang M, Ao X, Chu J, Jiang T, Qin A, Zhang Z. A specific aggregation-induced emission-conjugated polymer enables visual monitoring of osteogenic differentiation. Bioactive Mater. 2020;5:1018–25.
16. Wang L, Li B, Xu F, Xu Z, Wei D, Feng Y, Wang Y, Jia D, Zhou Y. UV-crosslinkable and thermo-responsive chitosan hybrid hydrogel for NIR-triggered localized on-demand drug delivery. Carbohydr Polym. 2017;174:904–14.
17. Pandya AD, Øverbye A, Sahariah P, Gaware VS, Høgset H, Masson M, Høgset A, Mælandsmo GM, Skotland T, Sandvig K, et al. Drug-Loaded Photosensitizer-Chitosan Nanoparticles for Combinatorial Chemo- And Photodynamic-Therapy of Cancer. Biomacromolecules. 2020;21:1489–98.
18. Tsai WB, Chen YR, Li WT, Lai JY, Liu HL. RGD-conjugated UV-crosslinked chitosan scaffolds inoculated with mesenchymal stem cells for bone tissue engineering. Carbohydr Polym. 2012;89:379–87.
19. Goldmann WH. Biosensitive and antibacterial coatings on metallic material for medical applications. Cell Biol Int. 2021;45:1624–32.
20. Zhao Z, Gao W, Bai H. A mineral layer as an effective binder to achieve strong bonding between a hydrogel and a solid titanium substrate. J Mater Chem B. 2018;6:3859–64.
21. Chen C, Hao Y, Bai X, Ni J, Chung SM, Liu F, Lee IS. 3D printed porous Ti6Al4V cage: Effects of additive angle on surface properties and biocompatibility; bone ingrowth in Beagle tibia model. Mater Des. 2019;175:107824.
22. Chen C, Qiu ZY, Zhang SM, Lee IS. Biomimetic fibronectin/mineral and osteogenic growth peptide/mineral composites synthesized on calcium phosphate thin films. Chem Commun. 2011;47:11056–8.
23. Chen C, Lee I-S, Zhang S-M, Yang HC. Biomimetic apatite formation on calcium phosphate-coated titanium in Dulbecco's phosphate-buffered saline solution containing CaCl(2) with and without fibronectin. Acta Biomater. 2010;6:2274–81.
24. Chen Y, Gao A, Bai L, Wang Y, Wang X, Zhang X, Huang X, Hang R, Tang B, Chu PK. Antibacterial, osteogenic, and angiogenic activities of SrTiO(3) nanotubes embedded with Ag(2)O nanoparticles. Mater Sci Eng C Mater Biol Appl. 2017;75:1049–58.

25. Lee K, Kim EH, Oh N, Tuan NA, Bae NH, Lee SJ, Lee KG, Eom C-Y, Yim EK, Park S. Contribution of actin filaments and microtubules to cell elongation and alignment depends on the grating depth of micrograting. J Nanobiotechnol. 2016;14:35.
26. Ngandu Mpoyi E, Cantini M, Reynolds PM, Gadegaard N, Dalby MJ, Salmerón-Sánchez M. Protein Adsorption as a Key Mediator in the Nanotopographical Control of Cell Behavior. ACS Nano. 2016;10:6638–47.
27. Vigneault P, Naud P, Qi X, Xiao J, Villeneuve L, Davis DR, Nattel S. Calcium-dependent potassium channels control proliferation of cardiac progenitor cells and bone marrow-derived mesenchymal stem cells. J Physiol. 2018;596:2359–79.
28. De Witte TM, Fratila-Apachitei LE, Zadpoor AA, Peppas NA. Bone tissue engineering via growth factor delivery: From scaffolds to complex matrices. Regenerative Biomaterials. 2018;5:197–211.
29. Wang Z, Dong L, Han L, Wang K, Lu X, Fang L, Qu S, Chan CW. Self-assembled Biodegradable Nanoparticles and Polysaccharides as Biomimetic ECM Nanostructures for the Synergistic effect of RGD and BMP-2 on Bone Formation. Sci Rep. 2016;6:1–12.
30. Carvalho MS, Cabral JMS, da Silva CL, Vashishth D. Synergistic effect of extracellularly supplemented osteopontin and osteocalcin on stem cell proliferation, osteogenic differentiation, and angiogenic properties. J Cell Biochem. 2019;120:6555–69.
31. Depalle B, McGilvery CM, Nobakhti S, Aldegaither N, Shefelbine SJ, Porter AE. Osteopontin regulates type I collagen fibril formation in bone tissue. Acta Biomater. 2021;120:194–202.
32. Liu F, Wang X, Zheng B, Li D, Chen C, Lee I, Zhong J, Li D, Liu Y. USF2 enhances the osteogenic differentiation of PDLCs by promoting ATF4 transcriptional activities. J Periodontal Res. 2020;55:68–76.
33. Sordi MB, Curtarelli RB, da Silva IT, Fongaro G, Benfatti CAM, de Souza Magini R. Cabral da Cruz, A.C. Effect of dexamethasone as osteogenic supplementation in in vitro osteogenic differentiation of stem cells from human exfoliated deciduous teeth. J Mater Science: Mater Med. 2021;32:1–9.
34. Chen C, Li H, Kong X, Zhang S-M, Lee I-S. Immobilizing osteogenic growth peptide with and without fibronectin on a titanium surface: effects of loading methods on mesenchymal stem cell differentiation. Int J Nanomed. 2015;10:283–95.
35. Jeong J, Kim JH, Shim JH, Hwang NS, Heo CY. Bioactive calcium phosphate materials and applications in bone regeneration. Biomaterials Res. 2019;23:4.
36. Danciu TE, Adam RM, Naruse K, Freeman MR, Hauschka PV. Calcium regulates the PI3K-Akt pathway in stretched osteoblasts. FEBS Lett. 2003;536:193–7.
37. Kläning E, Christensen B, Sørensen ES, Vorup-Jensen T, Jensen JK. Osteopontin binds multiple calcium ions with high affinity and independently of phosphorylation status. Bone. 2014;66:90–5.

# Scheme

Scheme 1 is available in the Supplemental Files section

# Figures


**Figure 1**

The general observation of porous implants. (A) General observation of Ti discs and bullet-shaped cage; (B) Pore structures of bullet-shaped cages filled with CSMA and CSMA/$CaCO_3$ hydrogels

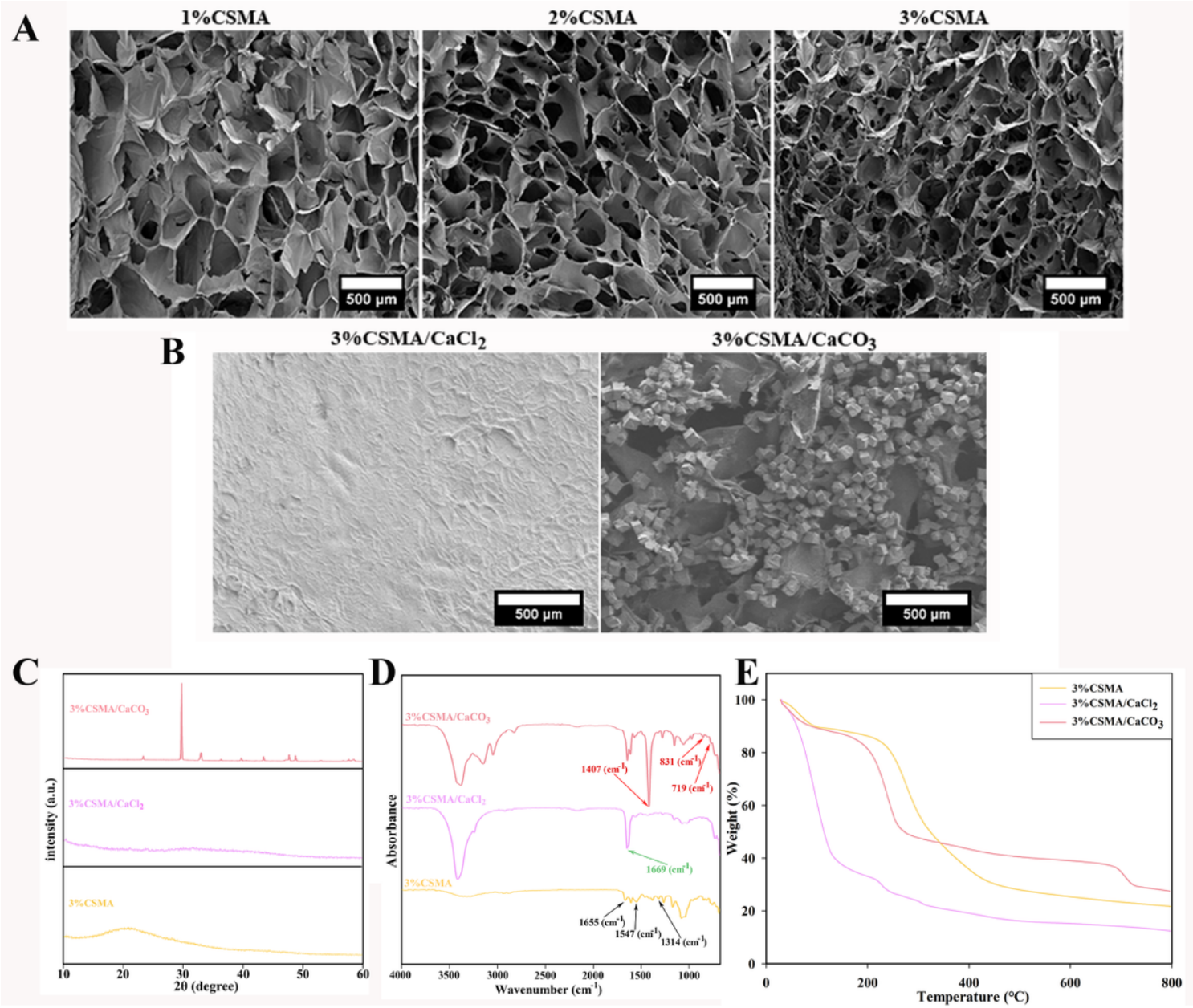


## Figure 2

Characterization of CSMA-based hydrogels. (A) SEM imsages of CMSA hydrogels with different chitosan concentration. (B) SEM imsages of 3% CSMA/$CaCl_2$ and 3%CSMA/$CaCO_3$ hydrogels. (C) AIR-FTIR spectra of 3% CSMA-based hydrogels. (D) XRD patterns of 3% CSMA-based hydrogels. (E) TGA of 3% CSMA-based hydrogels.

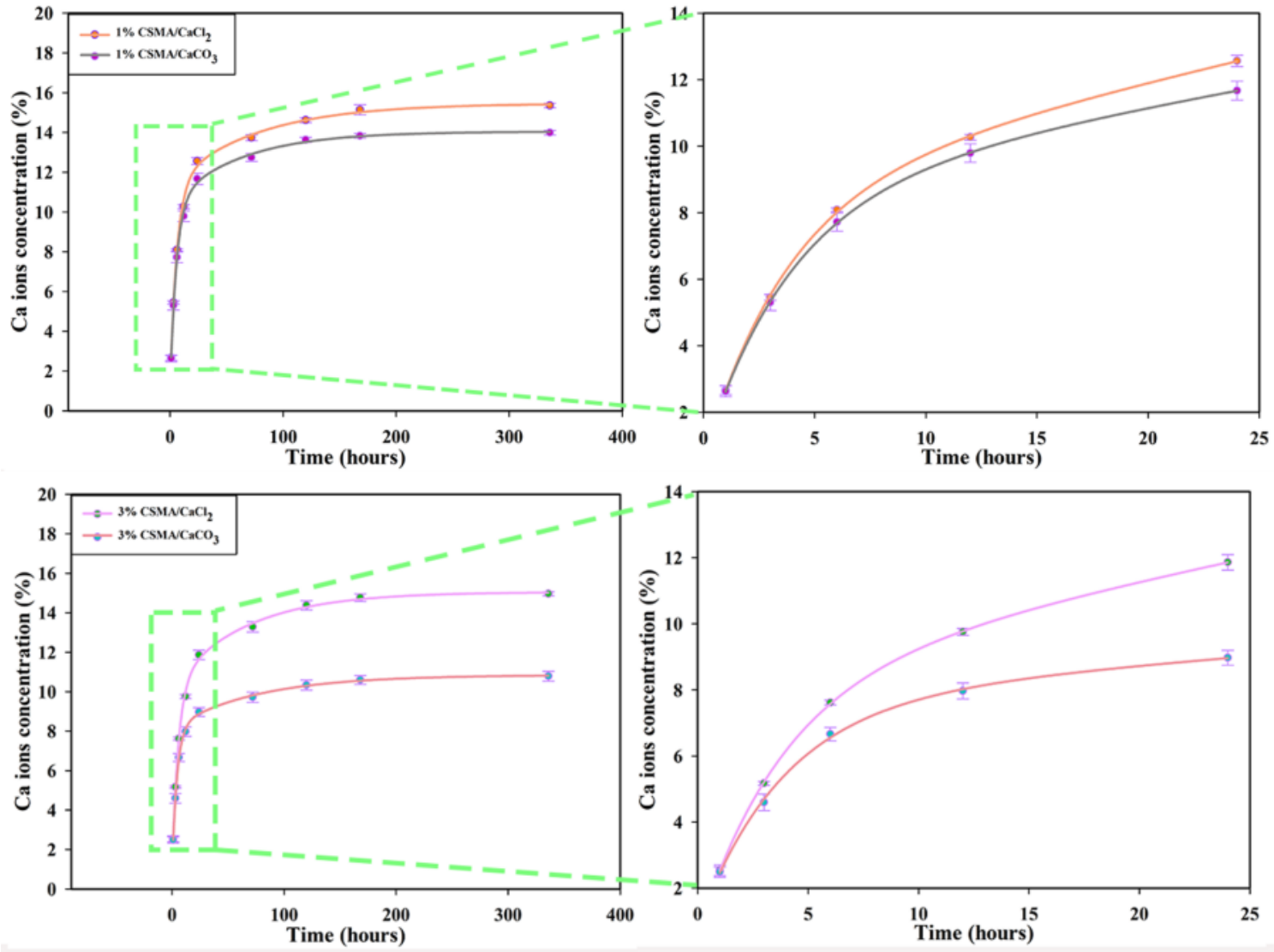


## Figure 3

The release prolife of $Ca^{2+}$ from CSMA-based hydrogels after immersion at different time points.

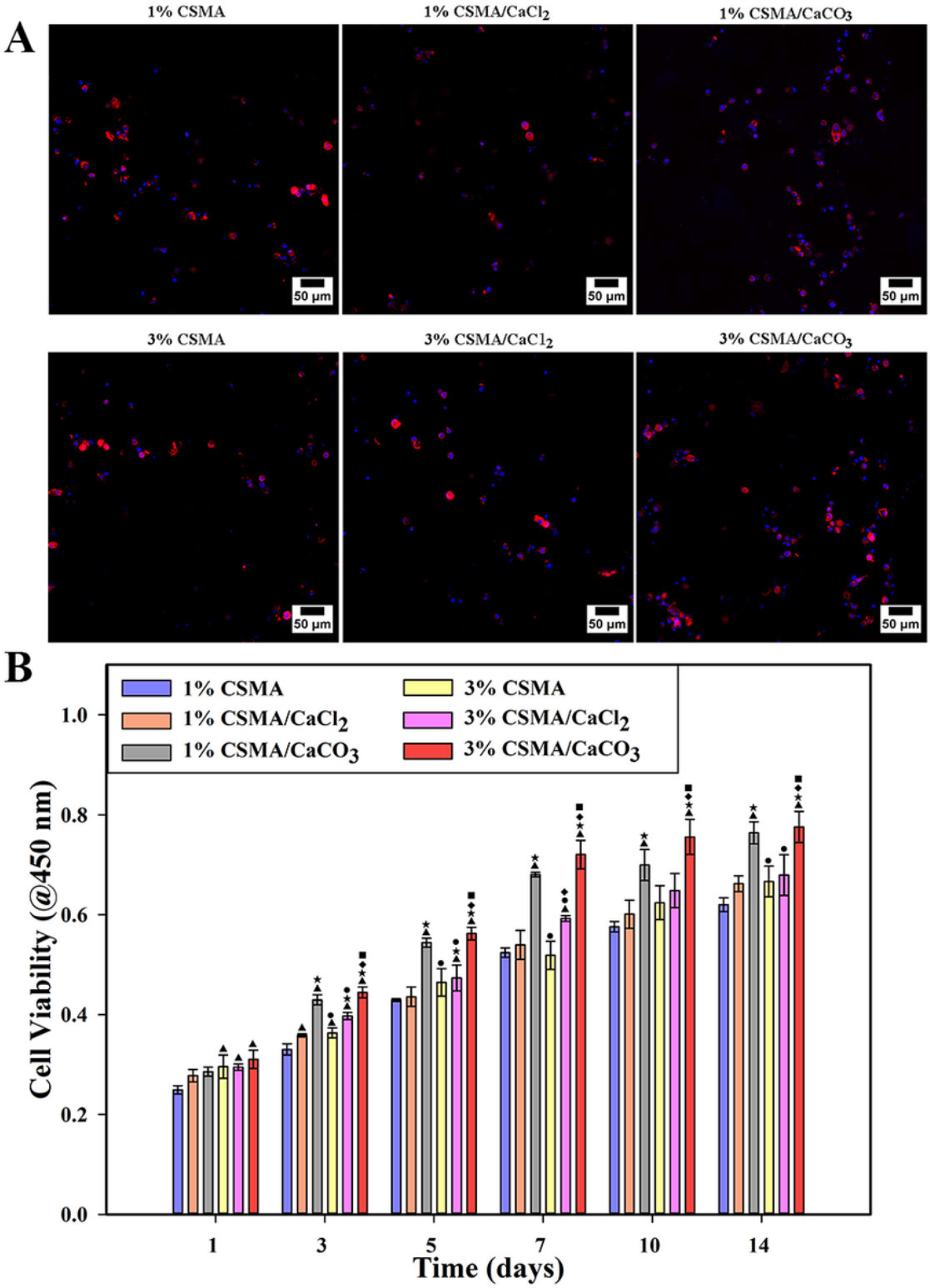


## Figure 4

BMSCs proliferation on CSMA-based hydrogels in growth medium for 14 days. (A) Confocal microscope images of cellular morphologies on CSMA-based hydrogels for 24 h. Cell membrane and nuclei were stained with DiI (red) and DAPI (blue), respectively. (Scale bar=50 μm). (B) Quantitative analysis of BMSCs proliferation by CCK-8. Values are represented as mean ± standard deviation (n = 3). (▲$P < 0.05$, as compared with the 1% CSMA, ▯$P < 0.05$, as compared with the 1% CSMA/$CaCl_2$, ●$P < 0.05$, as

compared with the 1% CSMA/$CaCO_3$, ▯$P < 0.05$, as compared with the 3% CSMA, ■$P < 0.05$, as compared with the 3% CSMA/$CaCl_2$).

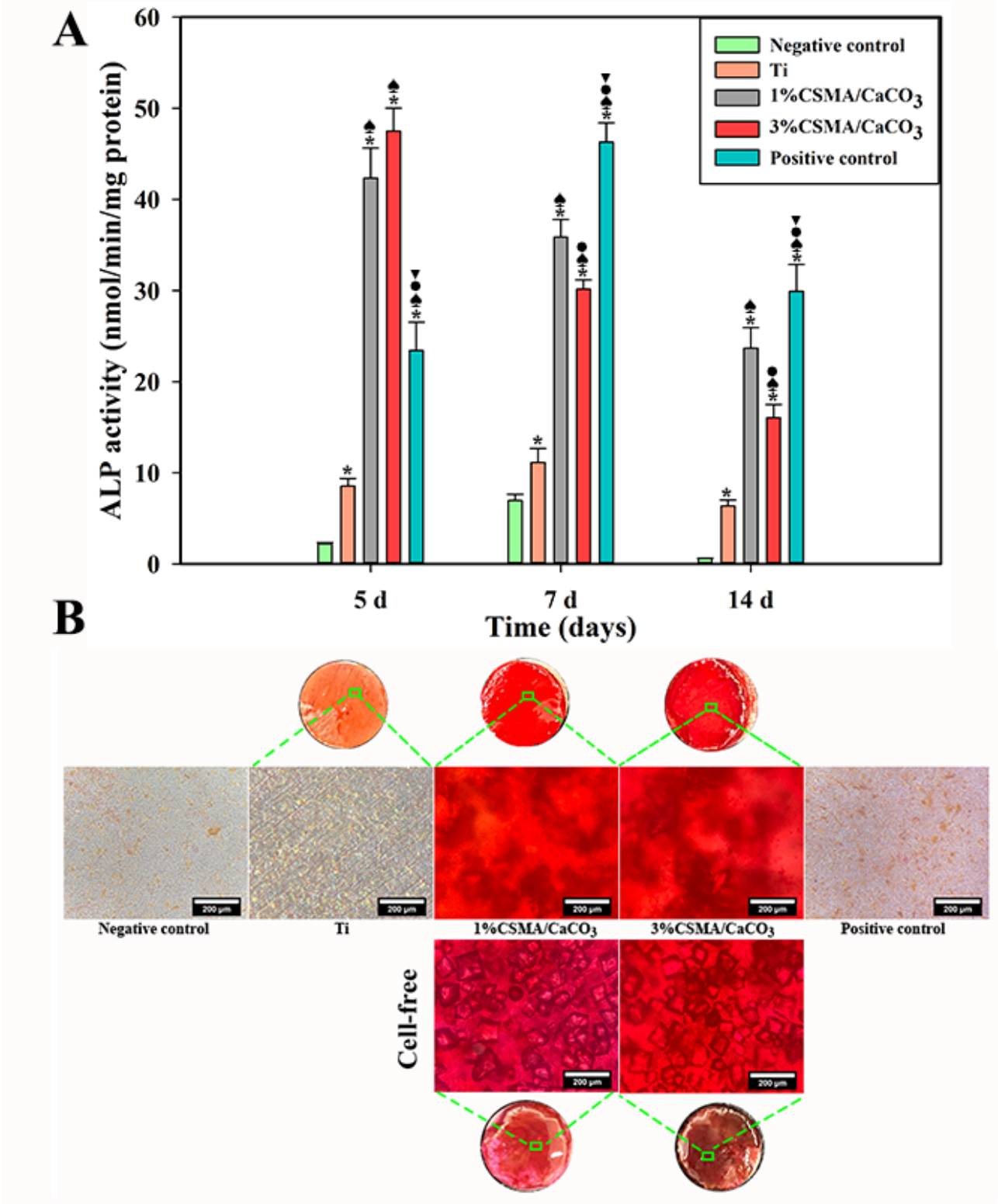


Figure 5

*In vitro* osteogenesis of BMSCs co-cultured on the Ti, 1% CSMA/$CaCO_3$ and 3% CSMA/$CaCO_3$ samples. (A) ALP activity of BMSCs in CSMA-based hydrogels at different time points. Values are represented as mean ± standard deviation (n = 3). (B) Alizarin Red staining images of BMSCs for 28 days. (*$P < 0.05$, as compared with the Negative control; ♠$P < 0.05$, as compared with the Ti; ●$P < 0.05$, as compared with the 1% CSMA/$CaCO_3$; ▼$P < 0.05$ , as compared with the 3% CSMA/$CaCO_3$).

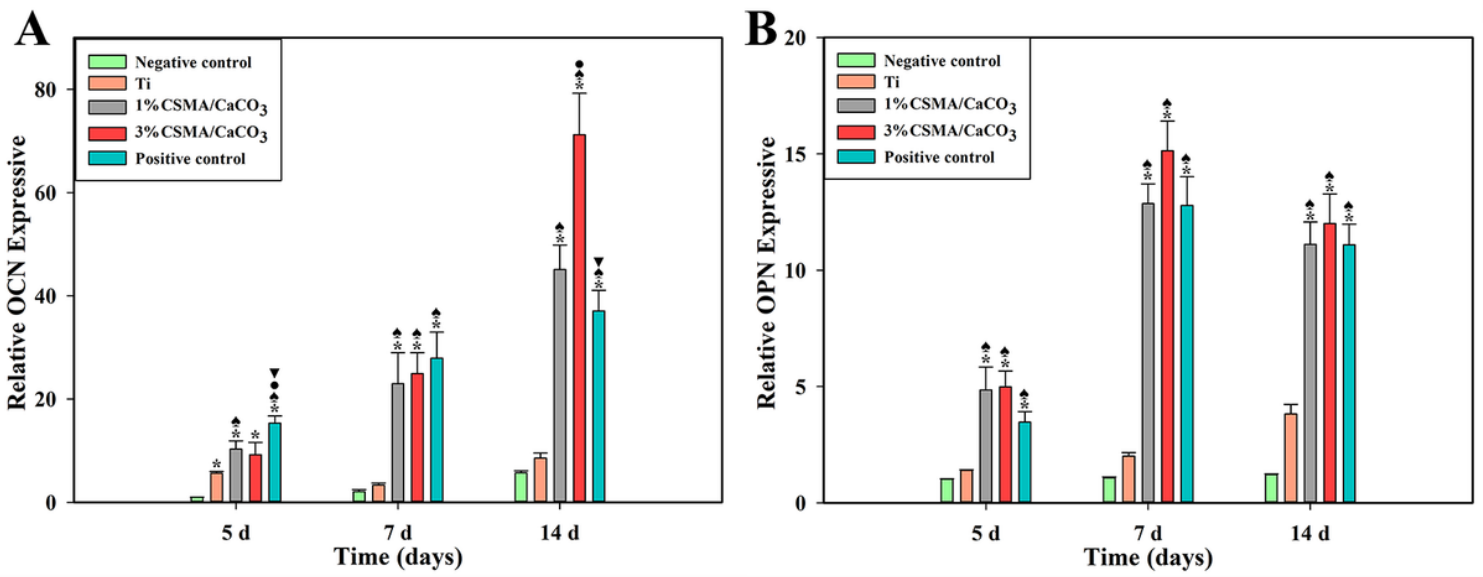


**Figure 6**

Osteogenesis-related gene expression levels of BMSCs co-cultured on the Ti, 1% CSMA/$CaCO_3$ and 3% CSMA/$CaCO_3$ samples by RT-PCR. The investigation of OCN (A) and OPN (B) levels at different time points. Values are represented as mean ± standard deviation (n = 3). (*$P < 0.05$, as compared with the Negative control; ♠$P < 0.05$, as compared with the Ti; ●$P < 0.05$, as compared with the 1% CSMA/$CaCO_3$).

## Supplementary Files

This is a list of supplementary files associated with this preprint. Click to download.

- Scheme1.png
- SupportingInformation2022211.docx